Electronic Supplementary Information

Alkynylation of Graphene via Sonogashira C-C Cross Coupling Reaction on Fluorographene

Demetrios D. Chronopoulos,[a] Miroslav Medveď,[a] Piotr Błoński,[a] Zdeněk Nováček,[b] Petr Jakubec,[a] Ondřej Tomanec,[a] Aristides Bakandritsos,[a] Veronika Novotná,[b] Radek Zbořil[a] and Michal Otyepka[a]*

[a]Regional Centre for Advanced Technologies and Materials, Department of Physical Chemistry, Faculty of Science, Palacký University Olomouc, 17. listopadu 1192/12, 771 46 Olomouc, Czech Republic
[b]NenoVision s.r.o., Purkyňova 649/127, 612 00 Brno, Czech Republic

1 Experimental studies

1.1 Materials

Fluorinated graphite (C:F, 1:1), alkynes (Phenylacetylene, Phenylethynyl magnesium bromide, 1-Phenyl-1-propyne, 4-Ethynylaniline, 5-Ethynylpyrimidine and 4-[(Trimethylsilyl)ethynyl]aniline, Bis(triphenylphosphine)palladium(II) dichloride [$Pd(Ph_3P)_2Cl_2$], Copper iodide (CuI), and dry N,N-dimethylformamide (DMF) were purchased from Sigma-Aldrich. All reagents were used as received without further purification.

1.2 Experimental section

In Sonogashira coupling reaction, bis(triphenylphosphine)palladium(II) dichloride [$Pd(Ph_3P)_2Cl_2$] (35.1 mg, 0.05 mmol) and copper iodide (CuI) (19 mg, 0.10 mmol) were solubilized in 2 mL dry N,N-dimethylformamide (DMF), under oxygen free conditions. Subsequently, suspension of FG (31 mg, ~1 mmol of C-F groups) sonicated for 4 h in 5 mL dry DMF was added to the above solution and the mixture was degassed by a stream of nitrogen. Afterwards, 1.2 eq. of alkyne (1.2 mmol) and triethylamine (Et_3N) (2 mL) were added to the suspension consecutively and the mixture was stirred at room temperature for 70 h, under nitrogen. Finally, the black product was separated by centrifugation and purified by repeated centrifugal washings with DMF, aqueous solution 5% HCl, water, ethanol and dichloromethane. The prepared graphene derivatives were dispersible in nonpolar solvents (toluene) but they tend to precipitate on longer time scales (days).

1.3 Section of control experiments

In order to investigate the role of each of reagents and catalysts participating in the Sonogashira reaction, many control experiments were performed applying the above mentioned reaction conditions. The progress of each reaction was monitored by FT-IR.

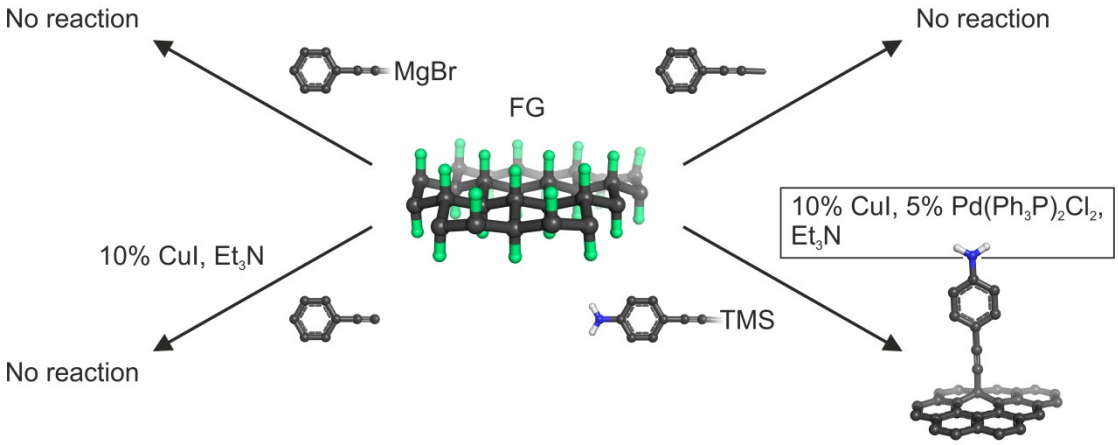

- The Grignard reaction of FG with phenylethynyl magnesium bromide, the Grignard reagent analogous to phenylacetylene, was also performed. The failure of the reaction demonstrated the uniqueness of the Sonogashira coupling for alkynylation of graphene.

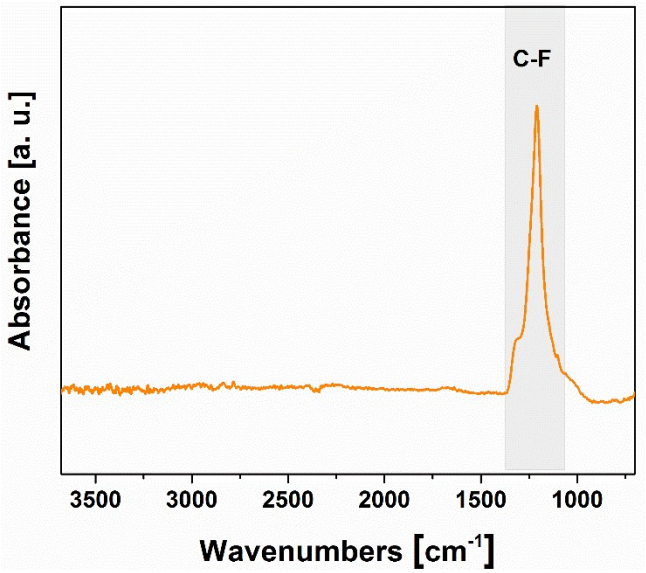

Figure S1. FT-IR spectrum of FG treated with the Grignard reagent (control experiment).

- The internal alkyne 1-phenyl-1-propyne was used instead of phenylacetylene, under the above mentioned conditions of the Sonogashira coupling. The unsuccessful reaction implies the necessity of terminal alkynes for the progress of the reaction.

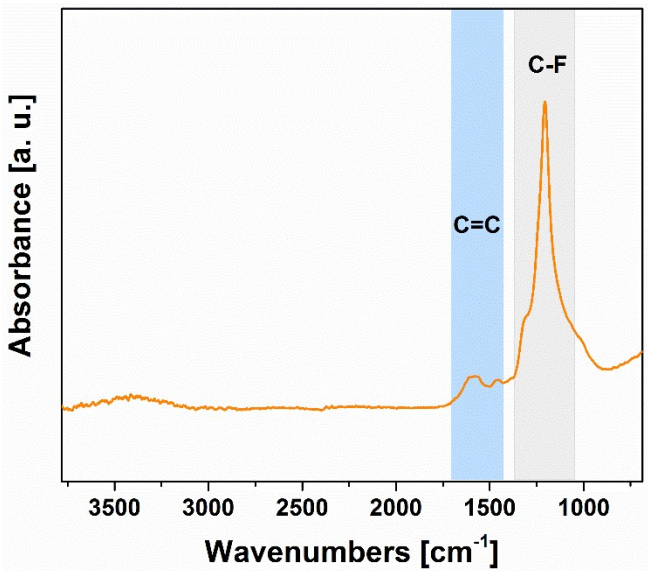

Figure S2. FT-IR spectrum of FG treated with the internal alkyne under the Sonogashira reaction conditions (control experiment).

- Since nucleophilic intermediates of the terminal alkynes are generated in situ in the Cu-cycle, the Sonogashira reaction was carried out using phenylacetylene as alkyne, skipping the step of the transmetalation. The negative result of the reaction indicated that all the steps of the Sonogashira mechanism are required for the successful modification of FG.

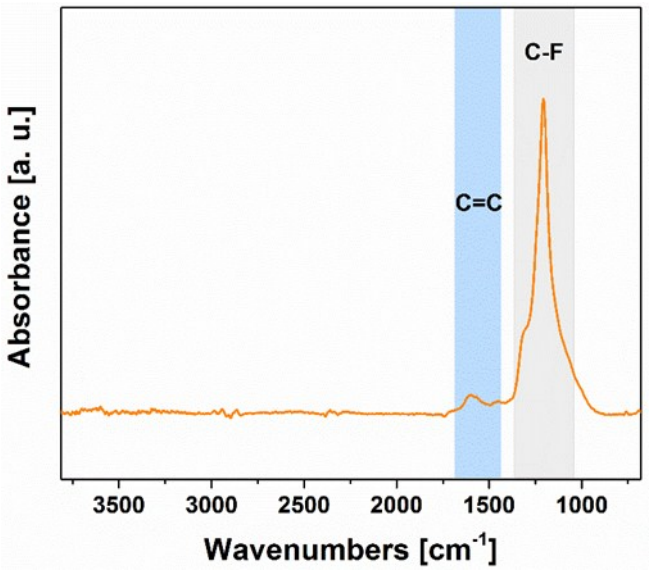

Figure S3. FT-IR spectrum of FG treated under conditions of the Cu-cycle of the Sonogashira reaction (control experiment).

- In the case of the control experiment with the internal alkyne, a low defluorination of FG was observed, with concurrent in situ generation of F anions in the solution. Since F anions can remove the protective silyl groups, forming in situ the corresponding terminal alkyne, the Sonogashira reaction was also performed between FG and 4-[(trimethylsilyl)ethynyl]aniline (TMS-Eta), a protective terminal alkyne. The reaction worked successfully, as in the case of non-protective terminal alkyne, showing that even the terminal protective alkynes can be employed for the covalent modification of FG.

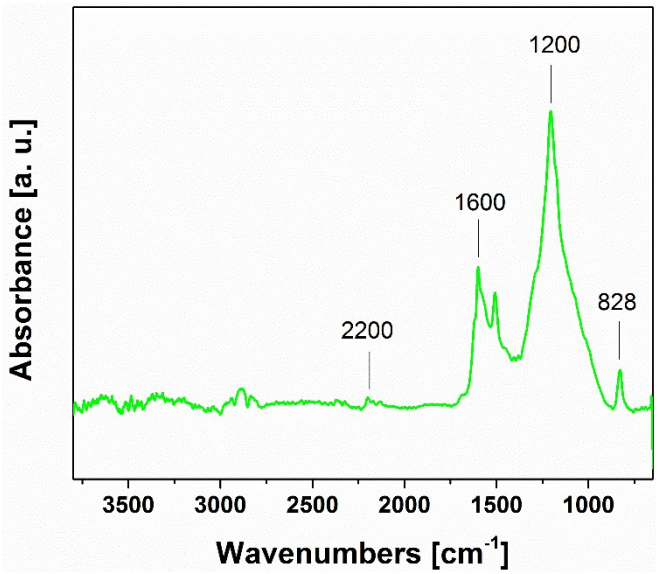

Figure S4. FT-IR spectrum of EtaG, prepared by Sonogashira reaction between FG and 4-[(Trimethylsilyl)ethynyl]aniline.

1.4 Instrumentation

FT-IR spectra were recorded on an iS5 FTIR spectrometer (Thermo Nicolet) using the Smart Orbit ZnSe ATR accessory. Briefly, a droplet of an ethanolic dispersion of the relevant material was placed on a ZnSe crystal and left to dry and form a film. Spectra were acquired by summing 52 scans recorded under a nitrogen gas flow through the ATR accessory. ATR and baseline correction were applied to the collected spectra. Raman spectra were recorded on a DXR Raman microscope using the 613 nm excitation line of a diode laser.

X-ray photoelectron spectroscopy (XPS) was carried out with a PHI VersaProbe II (Physical Electronics) spectrometer using an Al Kα source (15 kV, 50 W). The obtained data were evaluated with the MultiPak (Ulvac - PHI, Inc.) software package.

Electron microscopy images were obtained with a JEOL 2010 TEM equipped with a LaB6 type emission gun operating at 160 kV. STEM-HAADF (high-angle annular dark-field imaging) analyses for EDS (energy-dispersive X-ray spectroscopy) mapping of elemental distributions on the products were performed with a FEI Titan HRTEM operating at 80 kV. For these analyses, a droplet of an aqueous dispersion of

the material at a concentration of ~0.1 mg mL^{-1} was deposited on a carbon-coated copper grid and slowly dried at ambient temperature for 24 h to reduce its content of adsorbed water. AFM images were obtained in the amplitude modulated semicontact mode on an NT-MDT NTegra system equipped with a VIT-P AFM probe with the amplitude set point set to 71% of the free amplitude, a scanning speed of 0.5 Hz per line for all pictures, and using fresh cleaved muscovite mica.

Thermogravimetric analysis (TGA) with evolved gas analysis (EGA) was performed using a Netzsch STA 449C Jupiter thermo-microbalance coupled with a QMS 403C Aëolos quadrupole mass spectrometer. Measurements were carried out in an α-Al_2O_3 open crucible under N_2 flow. A temperature program from 40 to 1000 °C with heating rate of 10 °C min^{-1} was used. Before each experiment, the crucible was heated to 1340 °C and then cooled to room temperature. Masses in the range 12-100 *m*/*z* of the released gases for the G-Mal graphene derivative were determined with the mass spectrometer of the TGA instrument, starting at 100 °C to avoid overloading the spectrometer with adsorbed water.

Procedure for measuring conductivity of EtaG: Conductivity measurements were performed on TESCAN LYRA3 scanning electron microscope (SEM) equipped with NenoVision LiteScope™ atomic force microscope (AFM). SEM serves as a tool for precise navigation of the AFM tip to the selected micrometer-scale particles. The instrument enables 3D in-situ surface imaging, simultaneous SEM and AFM analysis using a unique patented Correlative Probe and Electron Microscopy™ imaging technique, depth or height profiling, precise tip navigation and local conductivity estimation. Gold plated contact mode silicon cantilevers were used as a local current probe. Once the tip is brought to contact, I/V spectroscopic curves are measured using LiteScope integrated current amplifier and corresponding software features. Amplifier input range is from -10 nA to +10 nA and the sample bias voltage can be swept from -10 V to +10 V.

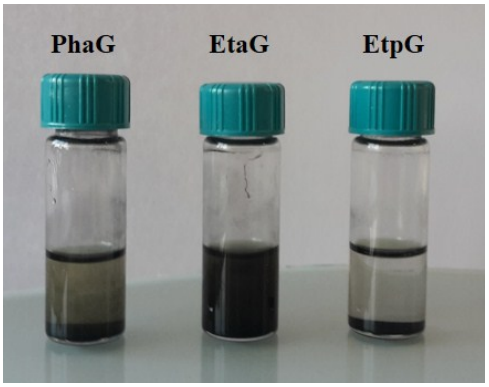

Figure S5. Digital images of alkynylated graphene derivatives (e.g. PhaG, EtaG, EtpG) dispersed in toluene. The materials were sonicated in the solvent for 1 h and rested for 24 h before capturing the images.

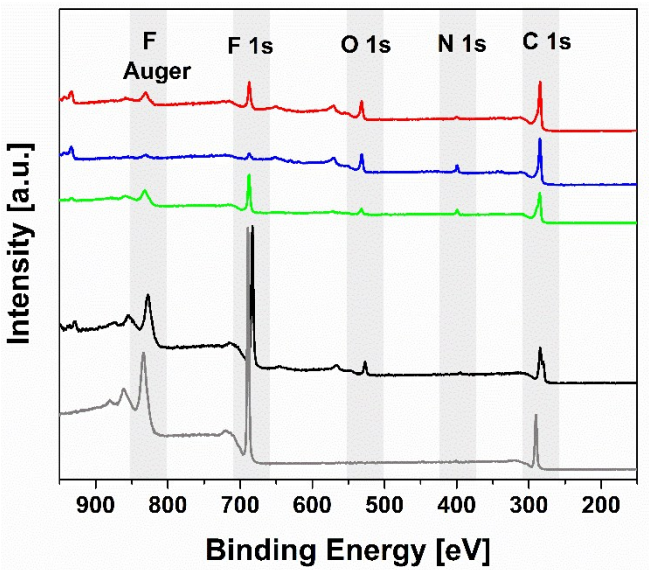

Figure S6. XPS survey spectra of PhaG (red), EtaG (blue), EtpG (green), treated FG after the Sonogashira reaction with internal alkyne (black) and pristine GF (grey).

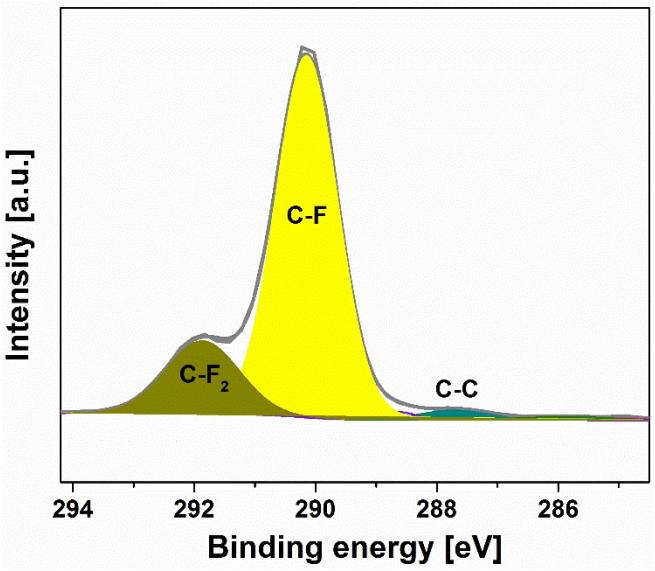

Figure S7. High resolution C 1s XPS spectrum of pristine GF.

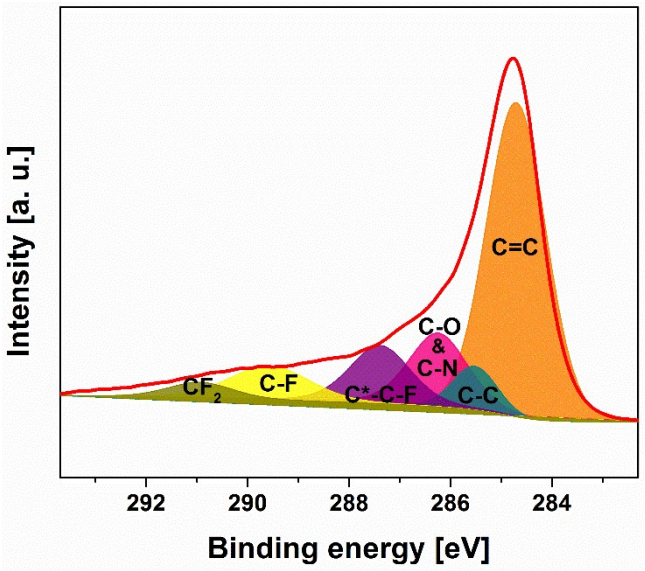

Figure S8. High resolution C 1s XPS spectrum of PhaG.

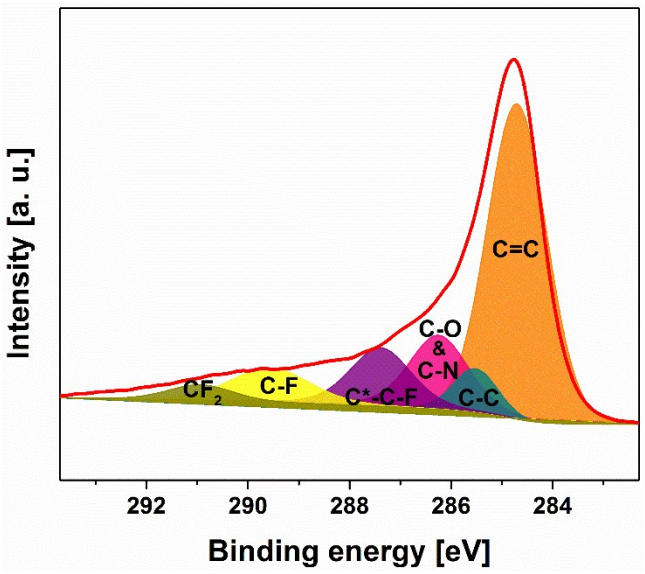

Figure S9. High resolution C 1s XPS spectrum of EtaG.

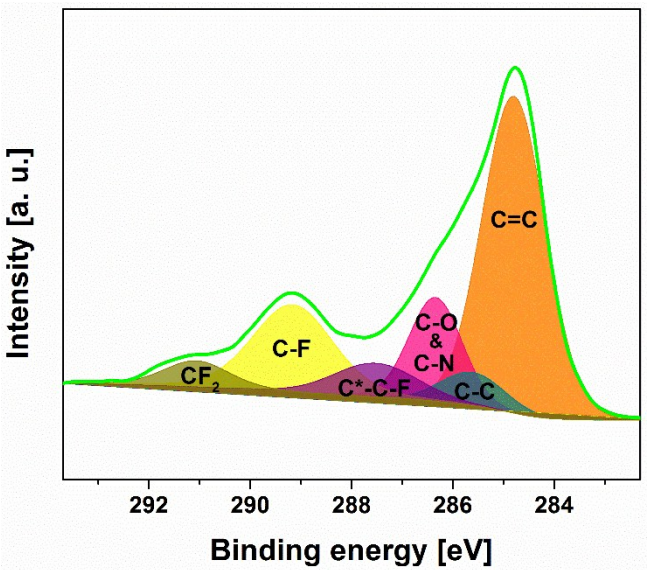

Figure S10. High resolution C 1s XPS spectrum of EtpG.

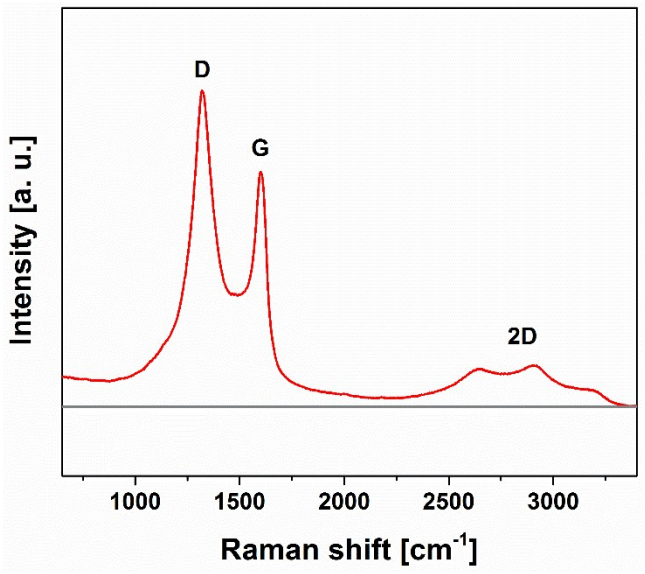

Figure S11. Raman spectra of pristine GF (gray) and PhaG (red).

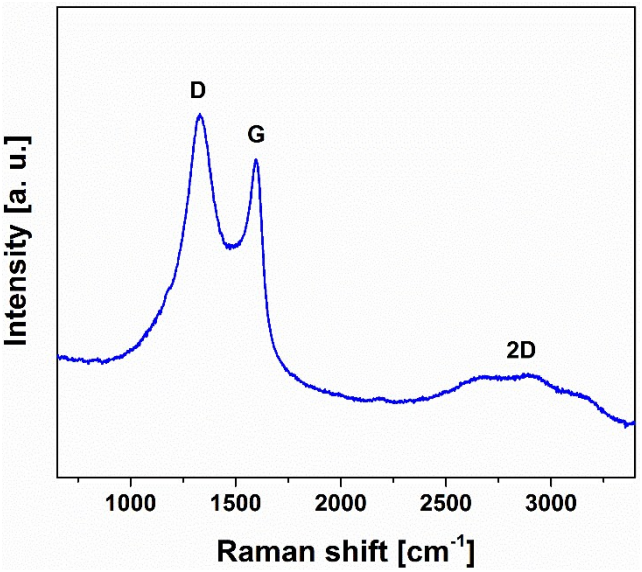

Figure S12. Raman spectrum of EtaG (blue).

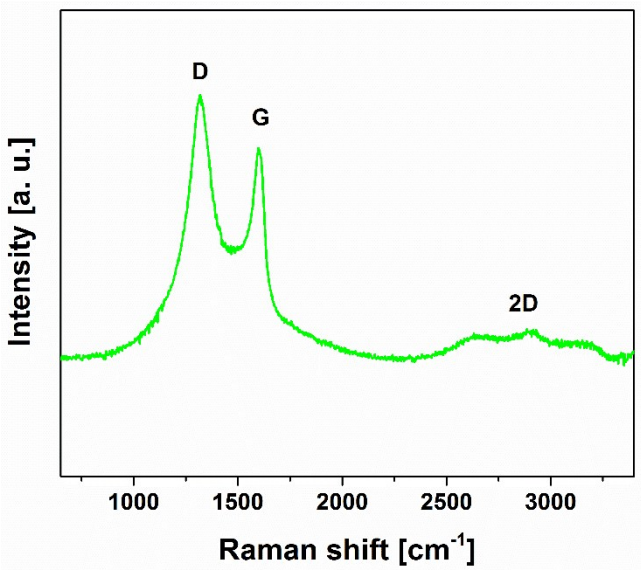

Figure S13. Raman spectrum of EtpG (green).

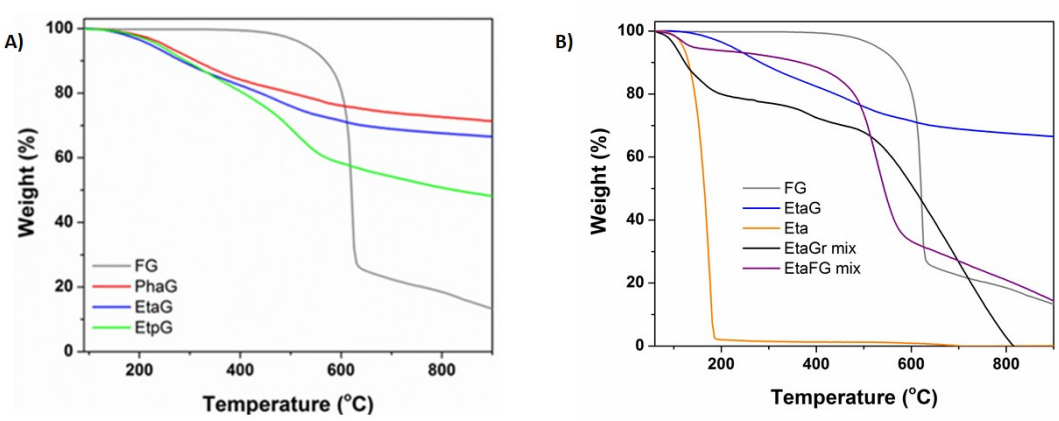

Figure S14. A) TGA graphs of graphite fluoride (grey), PhaG (red), EtaG (blue) and EtpG (green), and B) TGA graphs of FG, EtaG, and Eta, for confirming the covalent bonding between Eta and FG. EtaGr mix and EtaFG mix stand for samples prepared by drying of Eta with Graphene and FG, respectively. All the TGA graphs were obtained under N_2 atmosphere.

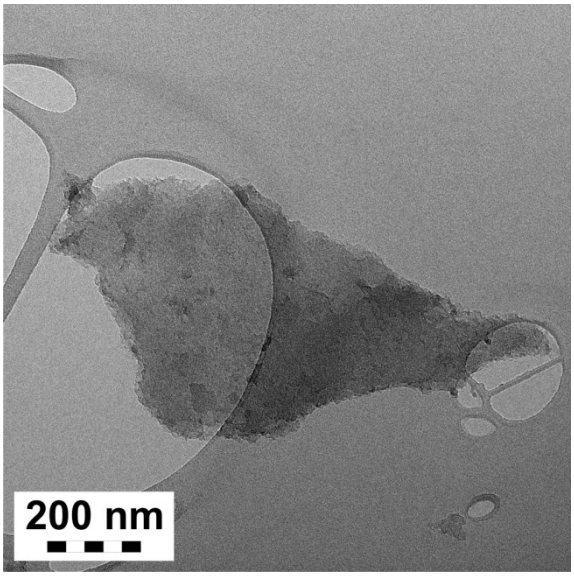

Figure S15. TEM image of **PhaG**.

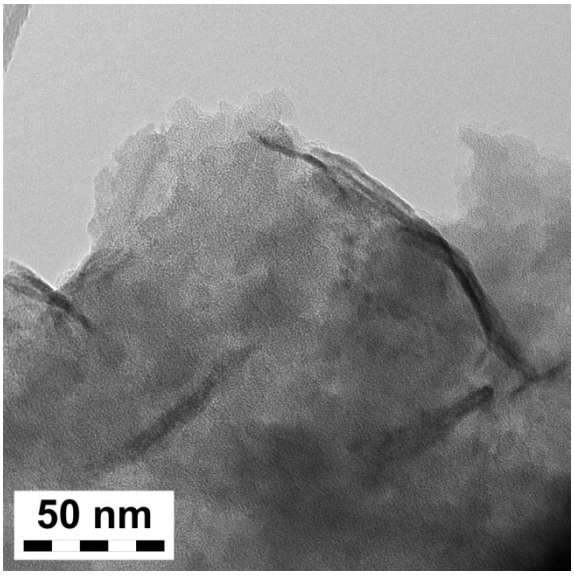

Figure S16. TEM image of **EtaG**.

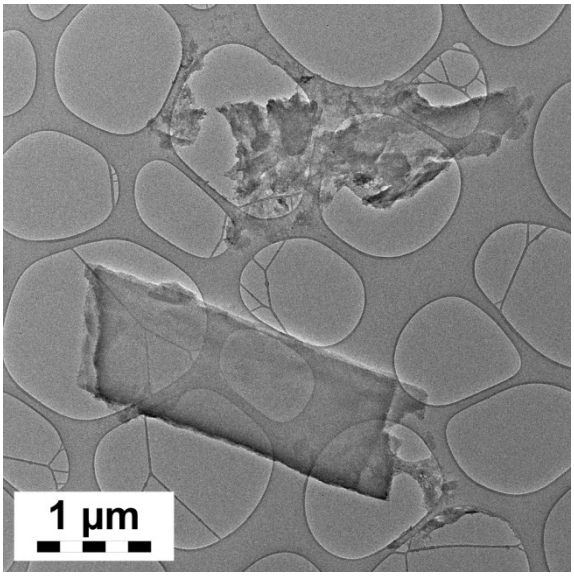

Figure S17. TEM image of **EtpG**.

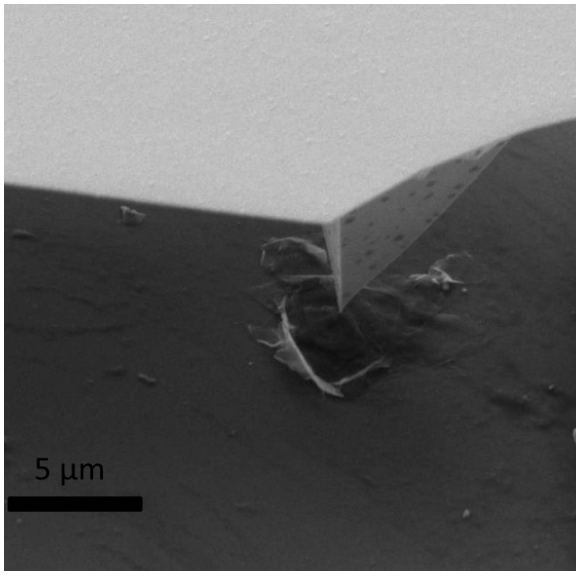

Figure S18. SEM image of **EtaG** from LiteScope™.

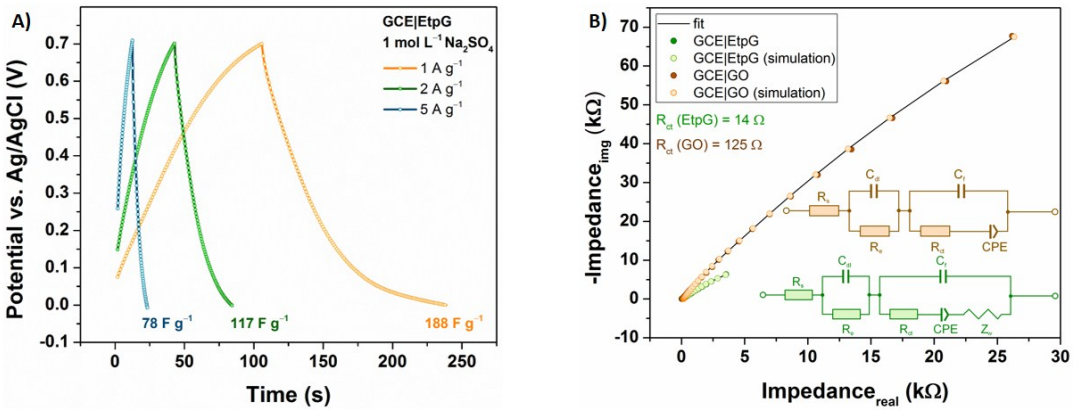

Figure 19. A) GCD curves of GCE modified with EtpG recorded at current densities ranging from 1 to 5 A g^{-1} in 1 mol L^{-1} Na_2SO_4 supporting electrolyte, and B) EIS spectra of EtpG and GO. The value of charge transfer resistance (Rct) for EtpG and GO are 14 and 125 Ohms.

Table S1. Elemental composition of chemically modified graphene derivatives, graphite fluoride (GF) and treated GF after Sonogashira reaction with the internal alkyne as obtained from the XPS analyses (wide scan XPS spectra).

		Atomic percentage [%]		
	C 1s (283 eV)	**N 1s** (400 eV)	**O 1s** (531 eV)	**F 1s** (686 eV)
PhaG	76.3	1.9	10.3	11.5
EtaG	76.6	7.6	12.5	3.3
EtpG	69.2	5.4	4.7	20.7
Blank experiment with internal alkyne	52.1	1.6	5.8	40.5
Graphite fluoride	43.5	0.24	0.24	55.7

Table S2. Determination of the different carbon components obtained from the deconvolution of the high resolution of C1s XPS spectra of the chemically modified graphene derivatives and of the pristine GF.

	C 1s bond dencovolution [%]					
	C=C (284.80-284.70 eV)	**C-C** (285.61-285.45 eV)	**C-O/C-N** (286.34-286.16 eV)	**C*-CF** (287.52-287.34 eV)	**C-F** (289.57-289.16 eV)	**CF_2** (291.07 eV)
PhaG	55.60	5.70	14.61	11.92	8.80	3.41
EtaG	61.11	6.29	16.11	10.86	5.63	-
EtpG	50.07	5.16	14.01	7.28	18.78	4.70
Graphite fluoride	0.29	0.89	-	2.31	77.50	18.00

2 Computational studies

2.1 Plane-Wave (PW) Density-Functional-Theory (DFT) Calculations with Periodic Boundary Condition (PBC)

PW-DFT-PBC calculations were performed by using the Vienna ab initio simulation (VASP) package.[1,2] A semi-local generalized gradient approximation (GGA) and the Perdew–Becke–Erzenhof (PBE) functional were employed [3,4] to account for electronic exchange and correlation effects. Atomic cores were represented by projected augmented wave potentials (PAW).[5,6] The PAW method is a genuine all-electron approach which produces the exact all-electron potentials and charge densities without elaborate nonlinear the necessity to include nonlinear corrections to the valence-core interactions. The PW basis set contained components with energies up to 400 eV, which allowed to achieve full basis-set convergence.

The graphene layer was represented by a periodically repeated conventional rectangular cell containing 192 C-atoms and 15 Å of vacuum, so that the interaction between the vertically repeated images was negligible. Up to six functional groups per computational cell uniformly distributed on the graphene layer were taken into account and both possible directions of adsorption were considered, i.e., under (bottom) and above (top) the graphene plane. For the sake of completeness, the adsorption of functional groups on a partially fluorinated graphene sheet containing twenty-two F-atoms per cell was also considered.

All the structures were fully optimized until the forces on all the atoms were smaller than 25 meV $Å^{-1}$. Simultaneously, the electronic degrees of freedom were relaxed until the change in total energy between successive iteration steps was smaller than 10^{-6} eV.

The Brillouin zone was sampled using $4 \times 4 \times 1$ Γ-centered *k*-point mesh and a Gaussian smearing of 0.02 eV. Electronic densities of states (DOS) were calculated by employing the tetrahedron method.[7] Local and partial DOS were obtained by projecting the plane-wave components onto spherical waves inside atomic spheres.

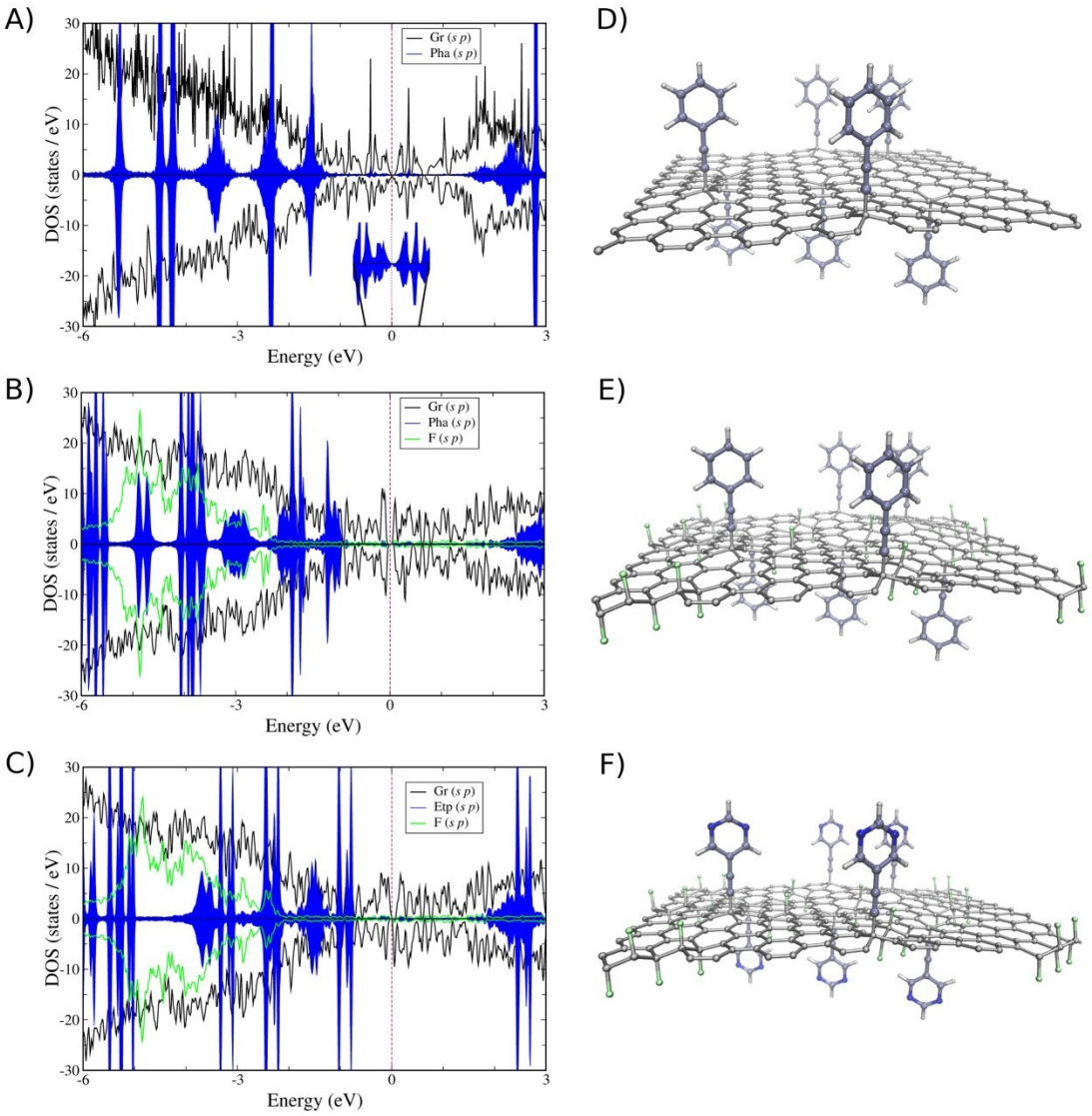

Figure S20. Partial DOSs and structural models applied in the computations: grafting Pha onto graphene (A, D), Pha onto partially fluorinated graphene (B, E) and Etp onto partially fluorinated graphene (C, F). The energies in DOSs are zeroed to the Fermi level. The inset in panel (a) shows a close-up of functional group states in the vicinity of E_F.

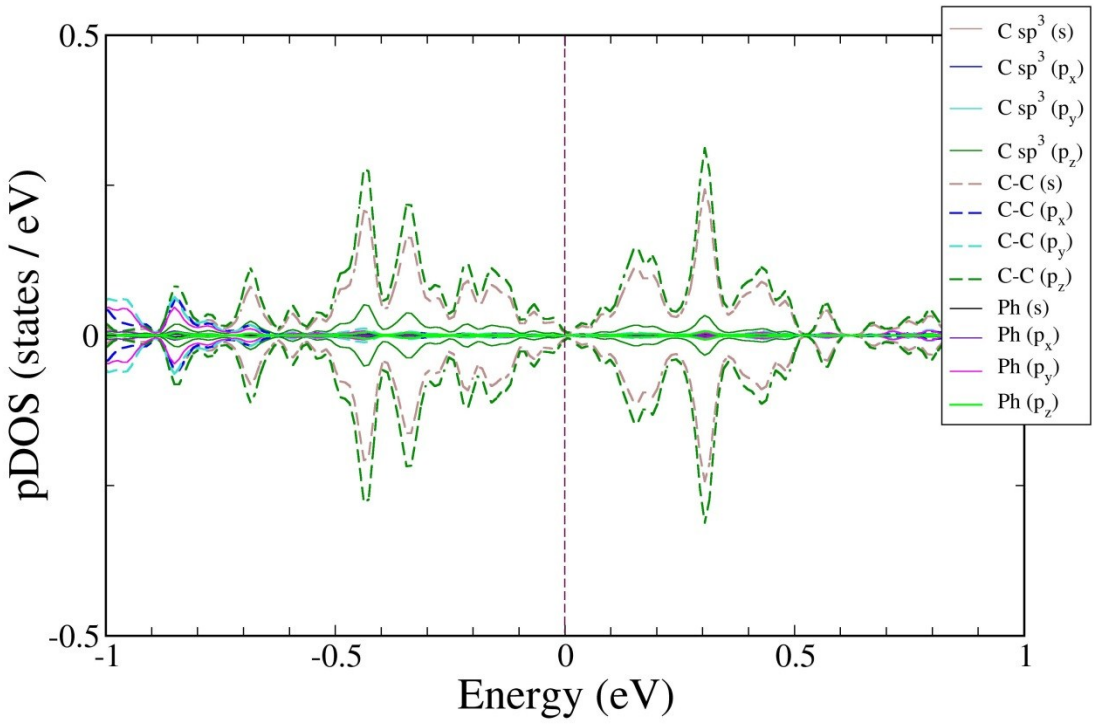

Figure S21. Partial DOSs of Pha grafted on graphene. The C sp^3 carbon atom lies in the graphene lattice, the C–C pair corresponds to the triple bond and Ph stands for phenyl. The energies are zeroed to the Fermi level.

2.2 Finite-size DFT Calculations

The ground state (GS) structures of all the investigated species were optimized by the ωB97X-D method [8] using the 6-31+G(d) basis set [9] for the 1st-3rd row elements and Stuttgart/Dresden (SDD) effective core potential (ECP) for palladium.[10] The selection of the ECP was based on a comparison of various ECPs in calculations of key binding parameters for model systems containing Pd—P and Pd—X (X = Cl, F) bonds (Table S3). For open-shell systems, the spin unrestricted formalism has been applied. The solvent effects were included by using the universal continuum solvation model based on solute electron density (SMD).[11]

Whereas the structures of small and medium size systems (HF, $Pd(PR_3)_2$, $Pd(PR_3)_2Cl^-$, R–C≡C–Cu, …) were fully relaxed in geometry optimizations, to mimic the semilocal flexibility of fluorographene (FG) sheets, the FG-like structures were obtained by constrained geometry optimizations relaxing only the region actively participating in a particular reaction, i.e. typically 4-6 carbons and 3-6 fluorine atoms. All calculations were performed with the Gaussian09 program.[12]

The optimized structures of model systems of the Pd catalyst and FG with different extent of fluorination are displayed in Figure S22 and S23, respectively. The FG model systems are fluoro-derivatives of ovalene (a polycyclic aromatic hydrocarbon containing 10 fused rings). Besides the shown FG model systems, fully fluorinated FG was considered referred to as c10-allF.

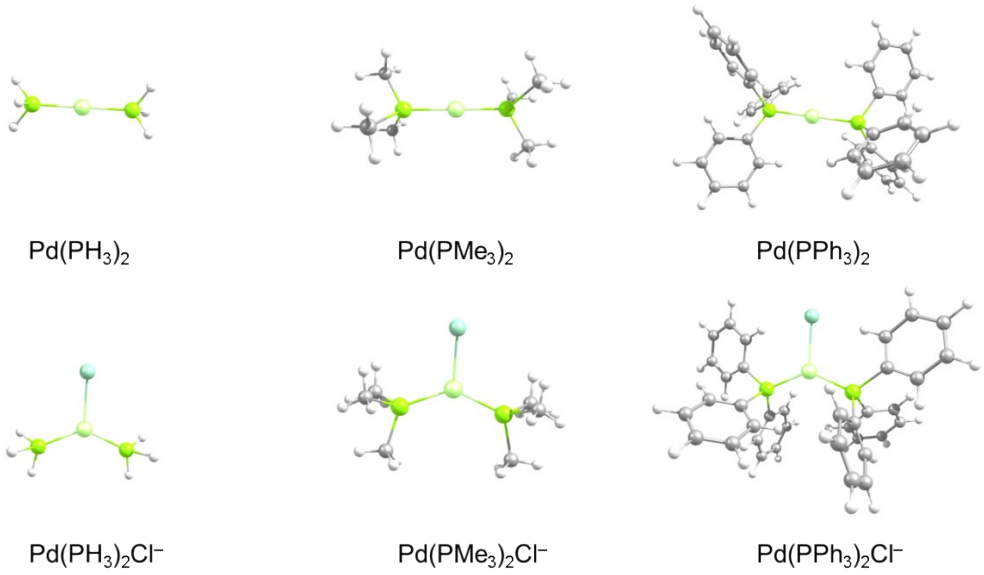

Figure S22. The gas phase structures of model systems of the catalyst optimized at the ωB97X-D/6-31+G(d)/SDD level of theory.

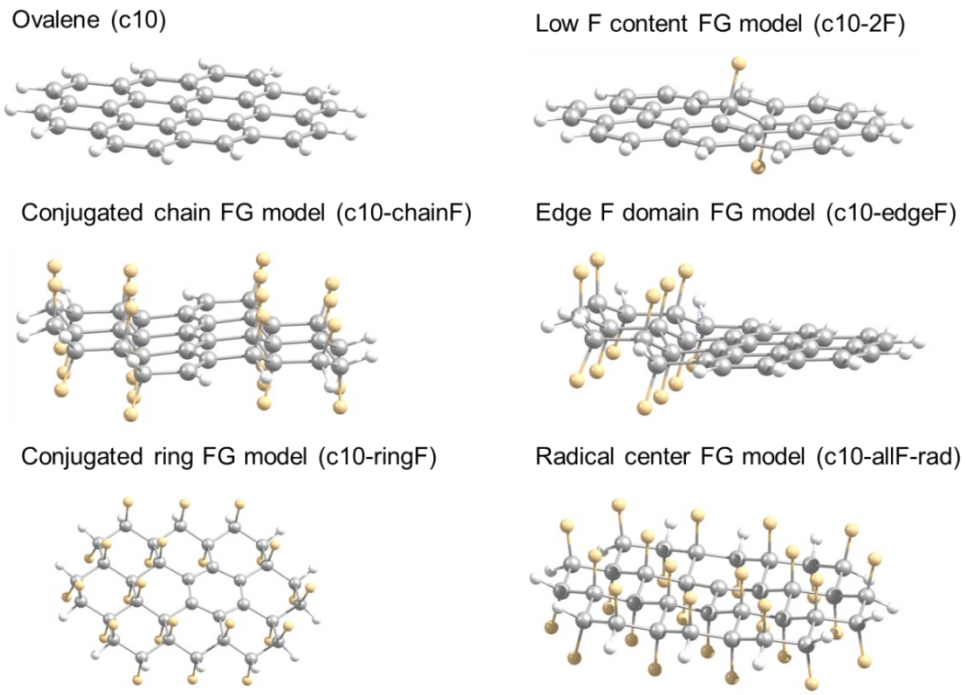

Figure S23. The gas phase structures of model systems of FG with different extent of fluorination optimized at the *ω*B97X-D/6-31+G(d)/SDD level of theory.

Table S3. Comparison of binding parameters including bond dissociation energy, bond lengths and Mulliken atomic charges for selected $Pd(PR_3)_2$ and $Pd(PR_3)_2X^-$ systems obtained at the ωB97X-D/6-31+G(d)/SDD level applying various ECPs for palladium.

System	6-31+G(d)/ Pd:ECP	BDE (Pd-X) [kcal/mol]	R(Pd-P) [Å]	R(Pd-X) [Å]	q(Pd) [e]	q(P) [e]	q(X) [e]
$Pd(PH_3)_2$	LANL2DZ	-29.1	2.30		0.02	-0.13	
	SDD	-30.9	2.29		0.36	-0.32	
	aug-cc-pVDZ-PP	-31.0	2.29		1.11	-0.70	
	aug-cc-pVTZ-PP	-31.8	2.28		1.12	-0.71	
$Pd(PPh_3)_2$	LANL2DZ	-25.1	2.33		0.35	-0.28	
	SDD	-25.3	2.31		0.48	-0.86	
	aug-cc-pVDZ-PP	-25.7	2.31		0.88	-0.83	
	aug-cc-pVTZ-PP	-26.4	2.30		-0.31	-0.42	
$Pd(PH_3)_2F^-$	LANL2DZ	-16.9	2.28	2.19	0.13	-0.16	-0.73
	SDD	-18.5	2.26	2.17	0.56	-0.40	-0.73
	aug-cc-pVDZ-PP	-21.0	2.26	2.15	1.00	-0.62	-0.72
	aug-cc-pVTZ-PP	-20.9	2.25	2.15	1.00	-0.67	-0.65
$Pd(PH_3)_2Cl^-$	LANL2DZ	-6.9	2.30	2.61	0.05	-0.18	-0.67
	SDD	-7.7	2.28	2.57	0.56	-0.41	-0.76
	aug-cc-pVDZ-PP	-9.1	2.27	2.54	1.02	-0.54	-0.94
	aug-cc-pVTZ-PP	-8.7	2.26	2.56	1.51	-0.87	-0.80
$Pd(PPh_3)_2F^-$	LANL2DZ	-27.3	2.30	2.33	-0.24	0.48	-0.61
	SDD	-28.4	2.29	2.29	0.50	-0.59	-0.59
	aug-cc-pVDZ-PP	-29.1	2.28	2.27	1.10	-0.76	-0.59
	aug-cc-pVTZ-PP	-29.1	2.27	2.27	-1.01	0.23	-0.58
$Pd(PPh_3)_2Cl^-$	LANL2DZ	-10.4	2.32	2.65	-0.28	0.59	-0.68
	SDD	-11.3	2.30	2.61	0.64	-0.67	-0.77
	aug-cc-pVDZ-PP	-12.2	2.30	2.60	1.29	-0.78	-0.81
	aug-cc-pVTZ-PP	-11.7	2.29	2.60	0.13	-0.31	-0.73

2.3 Binding modes of $Pd(PR_3)_2$ on FG (oxidative addition)

Table S4. Binding energies, C—Pd bond distances and Mulliken charges for model FG…$Pd(PR_3)_2$ systems calculated at the ωB97X-D/6-31+G(d)/SDD level (vacuum). The structures corresponding to local minima (in bold) are displayed in Figure S23.

System	BDE (FG…$Pd(PR_3)_2$) [kcal/mol]	*R*(C–Pd) [Å]	*q*(Pd) [e]	*q*(C) [e]	*Comment*
$Pd(PH_3)_2$					
c10…$Pd(PH_3)_2$	-4.3	~3.4	0.38	0.19	weakly bound
c10-2F...$Pd(PH_3)_2$	-1.8	~3.3			weakly bound
c10-edgeF...$Pd(PH_3)_2$	**-11.8**	2.21	0.34	-0.49	minimum
c10-chainF...$Pd(PH_3)_2$	**5.7**	2.21	0.36	-0.30	minimum
c10-ringF...$Pd(PH_3)_2$	10.4	~3.9			not bound
c10-allF-rad...$Pd(PH_3)_2$	**-10.0**	2.60	0.49	-0.65	minimum
c10-allF...$Pd(PH_3)_2$	13.5	~4.6			not bound
$Pd(PMe_3)_2$					
c10...$Pd(PMe_3)_2$	-5.1	~3.5			weakly bound
c10-2F...$Pd(PMe_3)_2$	-3.6	~3.7			weakly bound
c10-edgeF...$Pd(PMe_3)_2$	**-26.2**	2.21	0.65	-0.67	minimum
c10-chainF...$Pd(PMe_3)_2$	**-1.4**	2.20	0.34	-0.40	minimum
c10-allF-rad...$Pd(PMe_3)_2$	**-16.4**	2.98	1.04	-1.01	minimum
c10-allF...$Pd(PMe_3)_2$	12.0	~5.5			not bound
$Pd(PPh_3)_2$					
c10...$Pd(PPh_3)_2$	4.1	~3.8			weakly bound
c10-edgeF...$Pd(PPh_3)_2$	**-3.5**	~2.5			weakly bound
c10-chainF...$Pd(PPh_3)_2$	**-1.4**	~3.9			weakly bound
c10-allF-rad...$Pd(PPh_3)_2$	**-17.8**	2.94	1.08	-1.20	minimum
c10-allF...$Pd(PPh_3)_2$	2.1				weakly bound
$Pd(PH_3)_2Cl^-$					
c10...$Pd(PH_3)_2Cl^-$	NA				not bound
c10-2F...$Pd(PH_3)_2Cl^-$	NA				not bound
c10-edgeF...$Pd(PH_3)_2Cl^-$	-3.6	~4.1			weakly bound
c10-chainF...$Pd(PH_3)_2Cl^-$	13.8	~3.4			weakly bound
c10-allF-rad...$Pd(PH_3)_2Cl^-$	**-24.9**	2.73	0.50	-0.70	minimum
c10-allF...$Pd(PH_3)_2Cl^-$	NA				not bound
$Pd(PMe_3)_2Cl^-$					
c10-allF-rad...$Pd(PMe_3)_2Cl^-$	**-35.0**	3.18	1.02	-0.91	minimum
$Pd(PPh_3)_2Cl^-$					
c10-allF-rad...$Pd(PPh_3)_2Cl^-$	**-22.0**	3.07	1.31	-1.00	minimum

Table S5. Solvent effects on binding energies and C—Pd bond distances for model FG…$Pd(PMe_3)_2$ systems calculated at the ωB97X-D/6-31+G(d)/SDD level (gas phase vs. DMF).

	Vacuum		DMF	
System	**BDE (FG…$Pd(PR_3)_2$) [kcal/mol]**	***R*(C–Pd) [Å]**	**BDE (FG…$Pd(PR_3)_2$) [kcal/mol]**	***R*(C–Pd) [Å]**
$Pd(PMe_3)_2$				
c10...$Pd(PMe_3)_2$	-5.1	~3.5	-2.3	~3.8
c10-2F...$Pd(PMe_3)_2$	-3.6	~3.7	-3.8	~4.1
c10-edgeF...$Pd(PMe_3)_2$	**-26.2**	**2.21**	**-20.7**	**2.25**
c10-chainF...$Pd(PMe_3)_2$	**-1.4**	**2.20**	**3.5**	**2.20**
c10-allF-rad...$Pd(PMe_3)_2$	**-16.4**	**2.98**	**-17.9**	**3.31**
c10-allF...$Pd(PMe_3)_2$	12.0	~5.5	13.1	~5.5
$Pd(PMe_3)_2Cl^-$				
c10-allF-rad...$Pd(PMe_3)_2Cl^-$	**-35.0**	**3.18**	**-17.8**	**3.32**

Solvent effects have only a minor effect on the binding energy and intersystem distance for neutral FG…$Pd(PMe_3)_2$ complexes. On the other hand, the charged FG•…$Pd(PMe_3)_2Cl^-$ system is partly destabilized in DMF and its binding mode becomes very similar to the neutral complex suggesting that the presence of the Cl^- anion does not play an important role in the process.

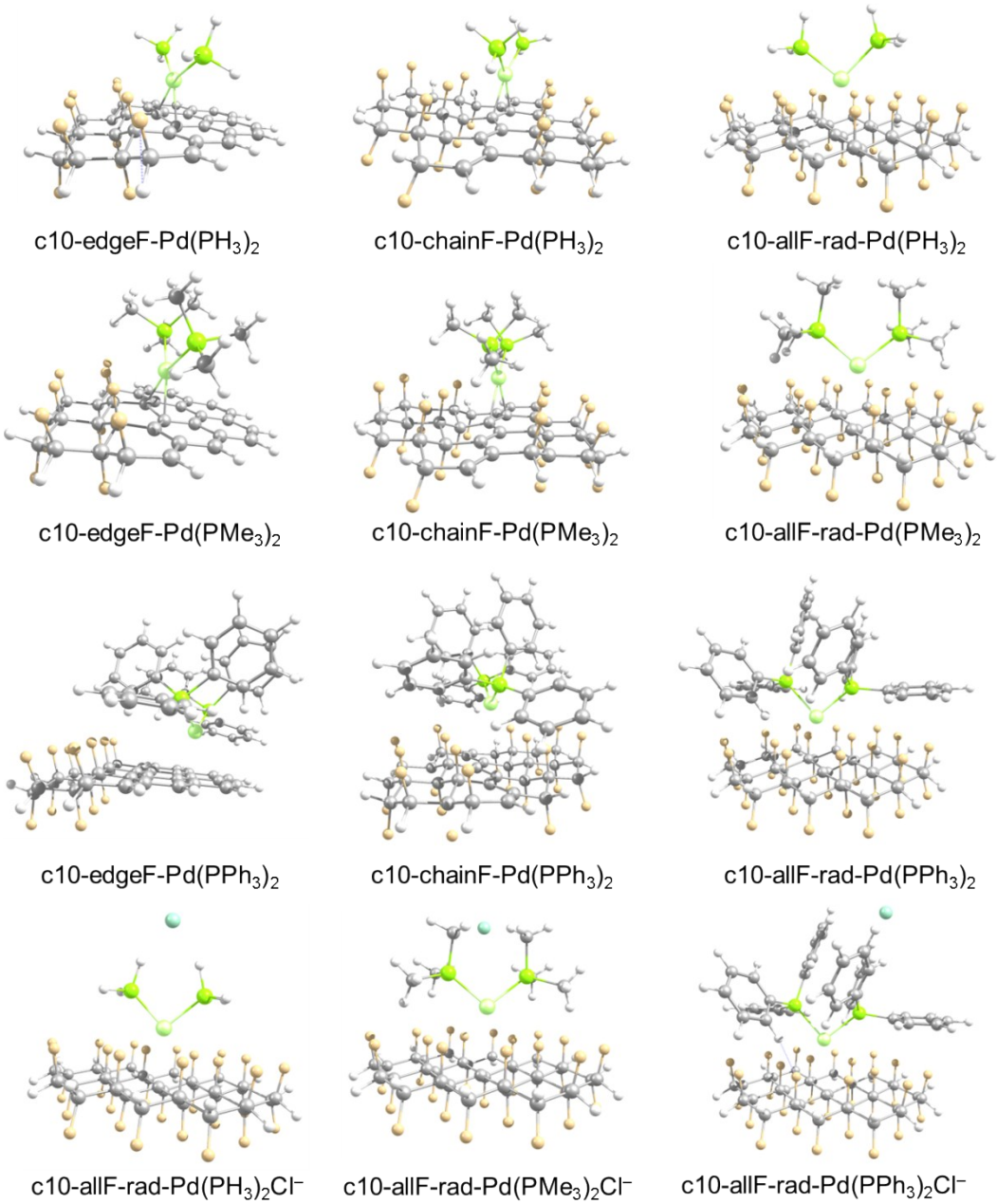

Figure S24. Binding modes of model systems of FG with the Pd catalyst obtained at the ωB97X-D/6-31+G(d)/SDD level of theory.

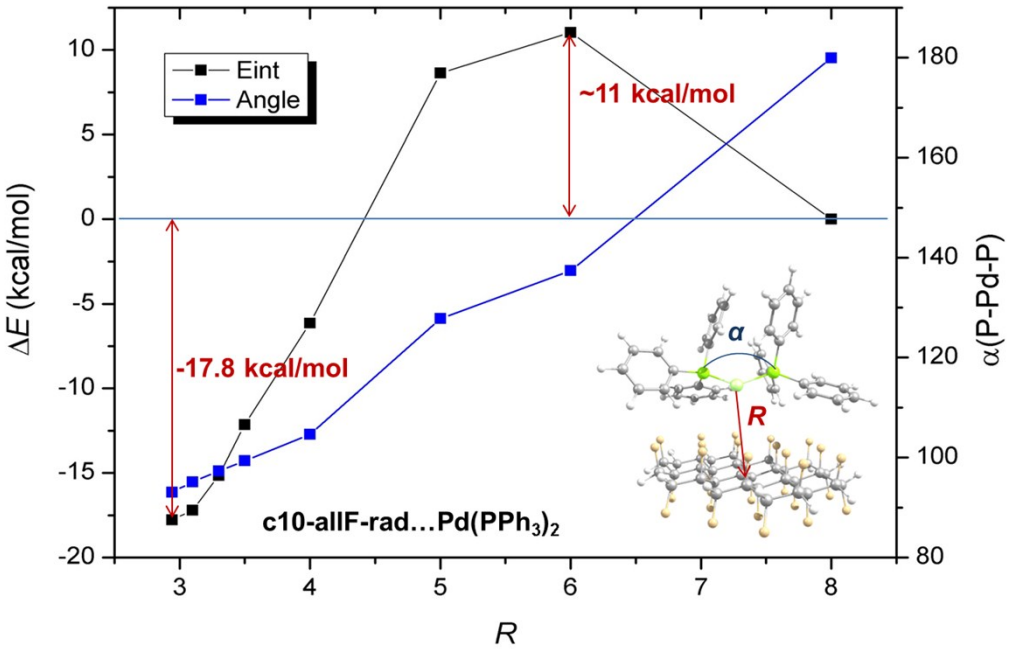

Figure S25. Dependence of the binding energy (kcal/mol) and the P–Pd–P bond angle for a model c10-allF-rad…$Pd(PPh_3)_2$ on the C—Pd interatomic distance *R* (in Å) calculated at the ωB97X-D/6-31+G(d)/SDD level (vacuum). The activation barrier for binding is ca. 11 kcal/mol; the bond angle decreases with decreasing distance from 180° (a linear alignment of isolated catalysts, cf. Figure S22) to 93.1° in the optimized complex.

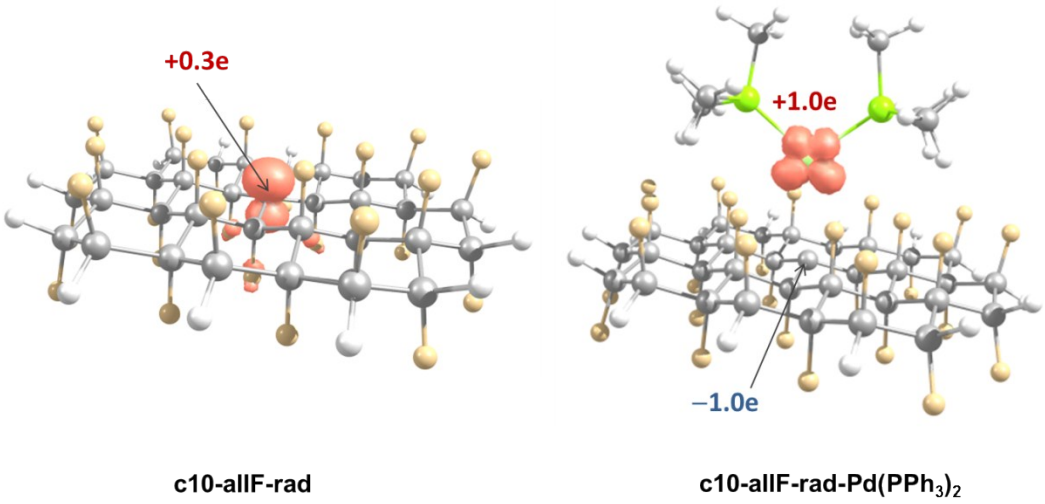

Figure S26. Charge transfer expressed in terms of spin density and Mulliken charge changes for model FG•…$Pd(PMe_3)_2$ systems calculated at the ωB97X-D/6-31+G(d)/SDD level (vacuum). The partial positive charge (+0.3e) on a radical center in FG• induced by the presence of fluorine atoms on neighboring carbons is changed to –1.0e in the complex. The electron transfer reflects also in the spin density redistribution; the unpaired electron in the complex is localized on palladium.

2.4 Formation of a fluoro-Pd(I)L_2-C(pFG) complex

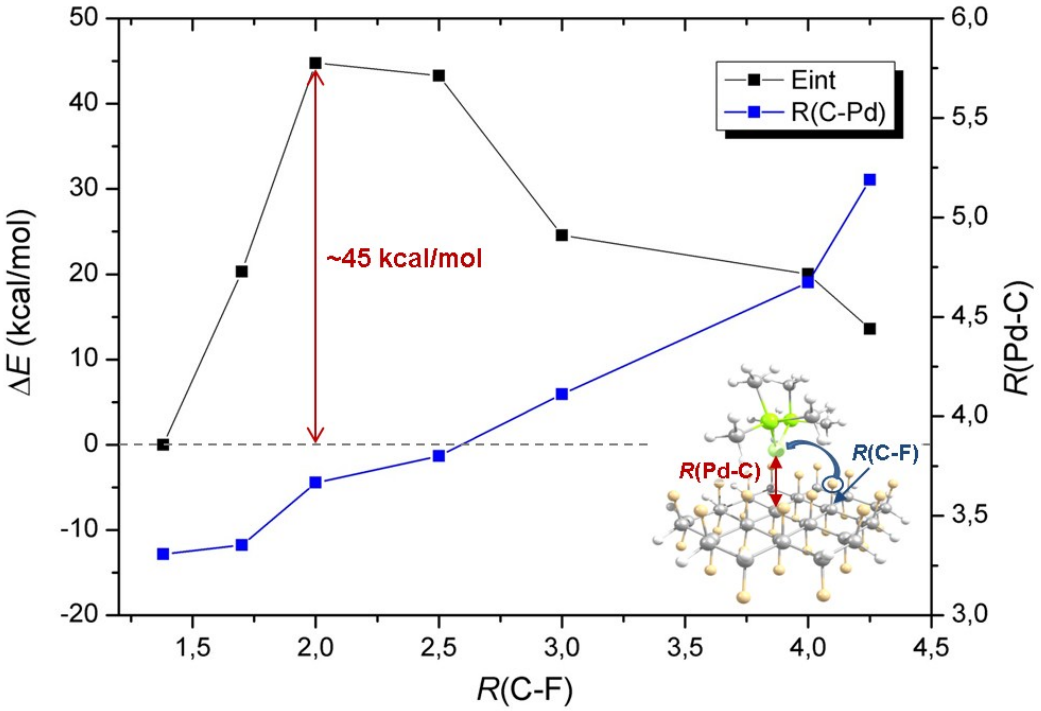

Figure S27. Energy profile (in kcal/mol) and intersystem distance (expressed in terms of *R*(Pd-C) in Å) dependence for the transfer of a fluoride anion from radical anion FG•⁻ to $Pd^{I}(PMe_3)_2$ as displayed in the inset calculated at the ωB97X-D/6-31+G(d)/SDD level (in DMF). The process is endothermic (ΔE = 13.6 kcal/mol) with a relatively high barrier ($\Delta E^{\#}$ = ~45 kcal/mol) discriminating this reaction path. The increasing value of *R*(Pd-C) (given in Å) indicates that this path would lead to detachment of the catalyst in the form of $Pd(PMe_3)_2F$.

2.5 Transmetalation and reductive elimination steps

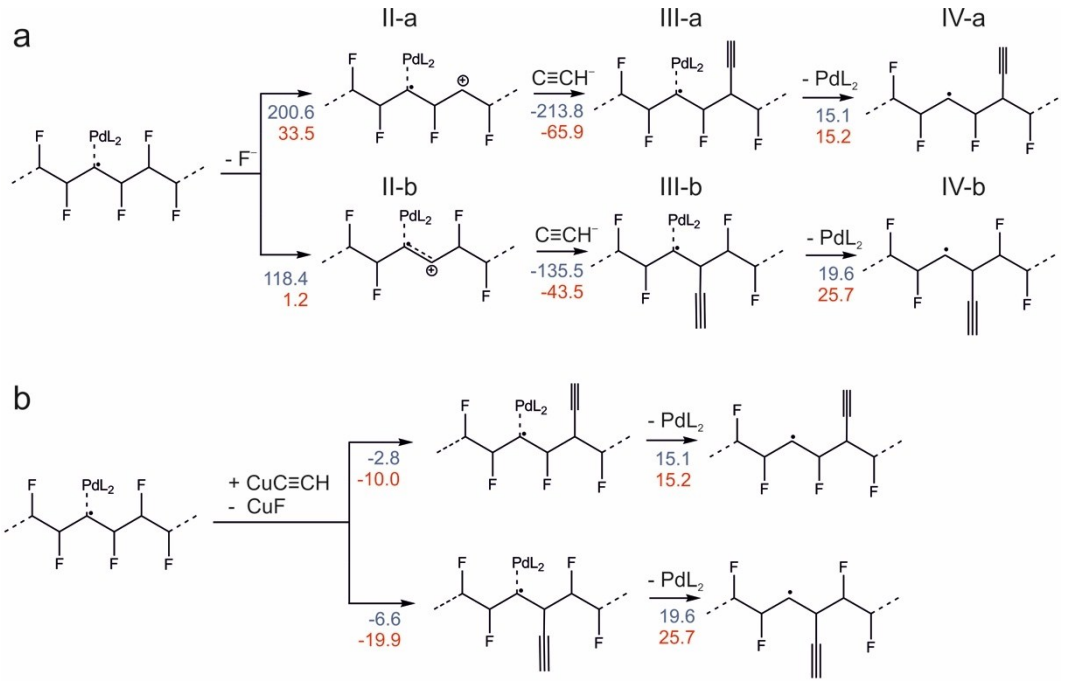

Figure S28. Proposed sequential mechanism of the transmetalation and reductive elimination steps of the Sonogashira cross-coupling reaction. (a) The path starts with detachment of a fluoride anion from pFG, proceeds with a nucleophilic attack by an alkynyl anion, and ends with detachment of the catalyst. (b) The same path involving copper species instead of the anions. The reaction energies (given in kcal/mol) were obtained at the ωB97X-D/6-31+G(d)/SDD level. Blue/red values correspond to the gas phase/DMF. Key structures are displayed in Figure S31.

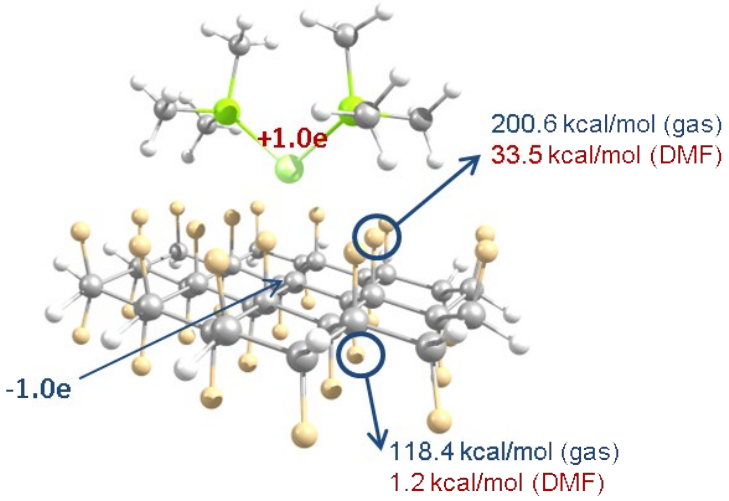

Figure S29. Fluoride anion detachment energies (in kcal/mol) for FG•…$Pd(PMe_3)_2$ calculated at the ωB97X-D/6-31+(d)/SDD level. Whereas the detachment is highly unfavorable in the gas phase, it is feasible in the solution mainly due to the stabilization of fluoride anion in polar solvents.

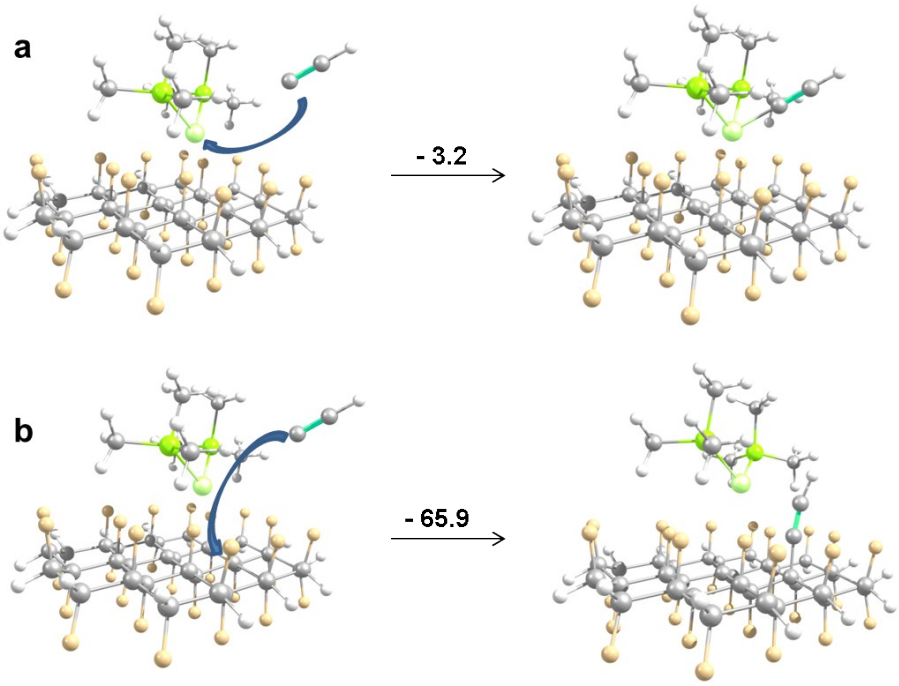

Figure S30. Comparison of binding energies (in kcal/mol) of an alkynyl group on positively charged FG•…$Pd(PMe_3)_2^+$ (formed by F^- detachment as depicted in Figure S28a) at the ωB97X-D/6-31+G(d) /SDD level in DMF. Clearly, the binding on pFG substrate is more favorable than the formation an alkynyl-$Pd(I)L_2$ complex.

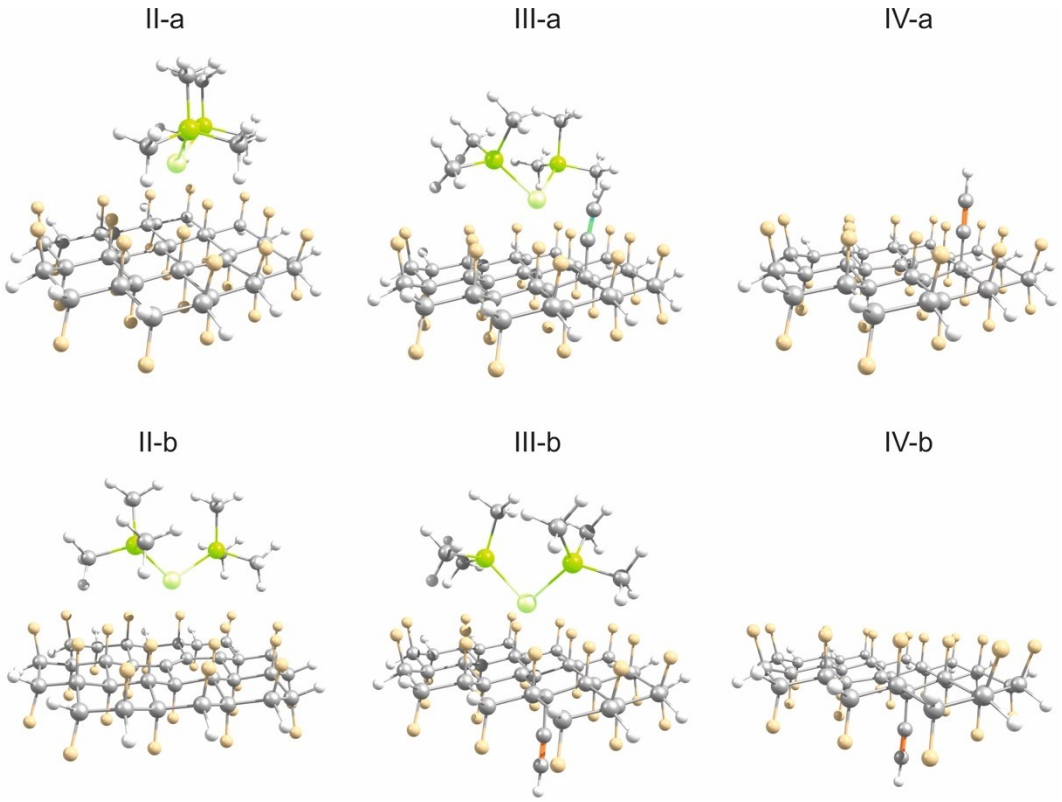

Figure S31. Key structures appearing in the sequential transmetalation mechanism (Figure S28) obtained at the ωB97X-D/6-31+G(d)/SDD level.

References

[1] G. Kresse and J. Furthmüller. Efficiency of ab-initio total energy calculations for metals and semiconductors using a plane-wave basis set. Comput. Mat. Sci., 6 (1996) 15.

[2] G. Kresse and J. Furthmüller. Efficient iterative schemes for ab initio total-energy calculations using a plane-wave basis set. Phys. Rev. B, 54 (1996) 11169.

[3] J. P. Perdew, K. Burke, and M. Ernzerhof. Generalized gradient approximation made simple. Phys. Rev. Lett., 77 (1996) 3865.

[4] J. P. Perdew, K. Burke, and M. Ernzerhof. Erratum: Generalized gradient approximation made simple. Phys. Rev. Lett., 78 (1997) 1396.

[5] P. E. Blochl. Projector augmented-wave method. Phys. Rev. B, 50 (1994) 17953.

[6] G. Kresse and D. Joubert. From ultrasoft pseudopotentials to the projector augmented-wave method. Phys. Rev. B, 59 (1999) 1758.

[7] P. E. Blöchl, O. Jepsen, and O. K. Andersen. Improved tetrahedron method for Brillouin-zone integrations. Phys. Rev. B 49 (1994) 16223.

[8] Chai, J.-D., Head-Gordon, M., Phys. Chem. Chem. Phys., 10 (2008) 6615-6620.

[9] Ditchfield, R; Hehre, W.J; Pople, J. A., J. Chem. Phys., 54 (1971) 724–728.

[10] Andrae, D.; Haeussermann, U.; M. Dolg, H. S.; Preuss, H., Theor. Chim. Acta, 77 (1990) 123-141.

[11] Marenich, A.V.; Cramer, Ch. J.; Truhlar, D. J., J. Phys. Chem. B, 113 (2009) 6378–6396.

[12] Frisch, M. J. et al. Gaussian09.D01, Gaussian Inc. Wallingford, CT, 2009.